Journal of Materials Chemistry A

PAPER

View Article Online
View Journal | View Issue

Published on 04 November 2016. Downloaded by Synchrotron Radiation Library on 11/09/2017 07:29:11.

Cite this: J. Mater. Chem. A, 2016, 4, 17848

Local heterojunctions of atomic Pt clusters boost the oxygen reduction activity of Rucore@Pdshell nanocrystallites†

Jeng Han Wang,[a] Kuan-Wen Wang,*[b] Tian-Lin Chen,[a] Chia-Hsin Wang,[c] Yu-Ming Huang,[d] Yang-Yang Hsu[d] and Tsan-Yao Chen*[de]

Received 15th August 2016
Accepted 31st October 2016

DOI: 10.1039/c6ta06995a

www.rsc.org/MaterialsA

Ru–Pd nanoparticles (NPs) with Pt atomic cluster modification were synthesized using polyol reactions with a sequence design. Such modification resulted in the formation of Ru in the inner core and Pd on the outer shell structure (Rucore–Pdshell) *via* transmetalation between the Pt ion and Pd atom followed by thermal reduction. The Pt modified Rucore–Pdshell NPs improve the on-set potential by 0.041 volt and reduce Pt loading to less than ~2%, as compared with that of carbon supported Pt NPs. For the optimum case, the MA (current degradation) of Ru–Pd NPs is improved (suppressed) by ~345% (18.1%) in the accelerated degradation test (ADT) at 0.85 volt (*vs.* RHE) for 5000 cycles by intercalating Pt clusters (2 to 9 at%) in the NP surface. These improvements are attributed to the electron localization and reinforcement by surface Pt clusters, which facilitated the oxygen reduction activity and chemical durability of NPs.

Introduction

Alkaline fuel cells (AFCs) are one of the robust energy technologies with cost-effective, eco-friendly, mass-productive, and durable properties at low operating temperature. The counter electrode (CE) incurs the highest capital cost (20–25%) in fabrication, the lowest chemical stability (due to the strong chemical corrosion), and the largest potential drift of an operating AFC. It conducts O_2 reduction, regenerating reaction sites at the anodic catalyst and thus completing the redox cycle. In a conventional AFC module, the cathode was fabricated by coating platinum nanoparticles on mesoporous conducting carbon materials (*e.g.*, carbon black, carbon nanotubes, or graphene). With this design, the fuel cell module achieved an impressive efficiency (up to ~65%); however, the high noble metal loading and the low reliability hindered its step into commercial markets.[1–4] The application of low cost transition metal alloys (*e.g.*, Co, Ni, Sn, and Pd) with a suitable carbon support (carbon nanotubes, active carbon, silver nanowires, or graphene)[5–7] at the cathode achieves considerable efficiency in AFCs. The implementation of these materials might be an optional solution to problems of cost. The limitations are the chemical durability in highly corrosive electrolytes and the complexity of fabrication processes which constrain their utility in the AFC cathode at the production level. Therefore, it is necessary to develop a cathodic catalyst with high redox kinetics and low chemical degradation, which can be commonly used reliably and cost-effectively. In this event, NPs comprising metal and metal oxide are suitable candidates. According to heterogeneous catalysis theory, the redox activity of NPs is dominated by their particle size, composition, geometric configuration, and lattice strain in near surface regions (Scheme 1).[8–13]

The fabrication techniques of NPs in a designed structure for high performance fuel cells have been extensively studied. Among the existing structural configurations, core–shell type NPs have superior activity and stability for oxygen reduction. Our previous studies have developed the capability to control the thickness of the shell crystal with atomic scale precision and the component of the core with interface homogeneity in tuneable electronegativity.[14–16] The intercalation of suitable atomic clusters to core–shell NPs is an effective heterogeneous modification for the improvement of stability and activity in long-term electrochemical reactions. In this study, atomic scale Pt clusters are intercalated to Ru–Pd (the schematic configuration is given in Scheme 1) NPs as the cathodic catalyst of AFCs. We demonstrate how Pt clusters extract electrons from the $Ru_C@Pd_S$ NPs underneath. This electron relocation facilitates the oxygen reduction activity and the chemical durability of NPs. For clarifying the charge localization effects on electrochemical performance, a control experiment was conducted using carbon supported bimetallic Ru–Pd NPs. In contrast to

[a]Department of Engineering and System Science, National Tsing Hua University, Hsinchu 30013, Taiwan
[b]Institute of Nuclear Engineering and Science, National Tsing Hua University, Hsinchu 30013, Taiwan
[c]Department of Chemistry, National Taiwan Normal University, Taipei 106, Taiwan
[d]Institute of Materials Science and Engineering, National Central University, Taiwan. E-mail: chencaeser@gmail.com; Tel: +886 3 5715131 ext. 34271
[e]National Synchrotron Radiation Research Center, Hsinchu 30013, Taiwan

† Electronic supplementary information (ESI) available: The ERXPS, VB spectra, *J–V* curves, and HRTEM images of reference materials are enclosed. See DOI: 10.1039/c6ta06995a

This journal is © The Royal Society of Chemistry 2016

Published on 04 November 2016. Downloaded by Synchrotron Radiation Library on 11/09/2017 07:29:11.

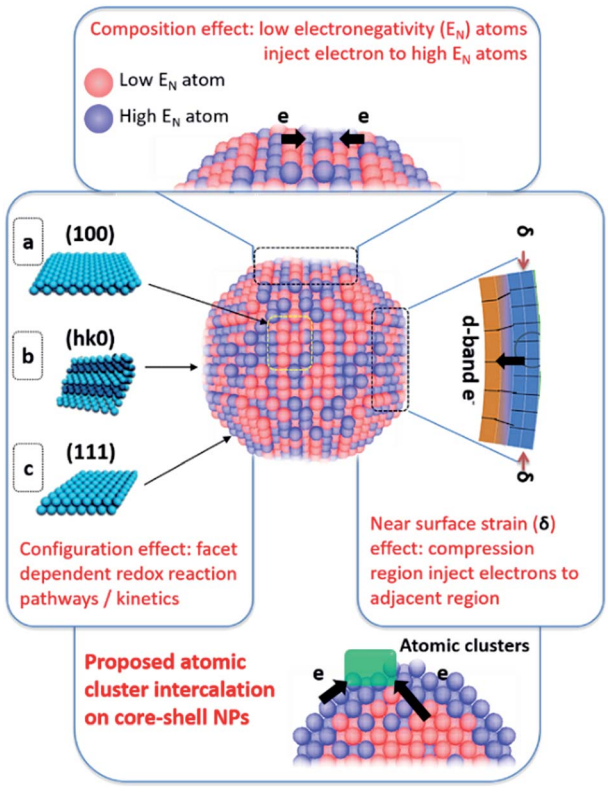

Scheme 1 Structural parameters that affect the redox activity of NPs and the schematic configuration of the proposed atomic cluster intercalation on core–shell NPs.[8–13]

the AFC with the Ru–Pd NP cathode, the $Ru_C@Pd_S$ with Pt modification ameliorated the on-set potential (V_{OC}) by 0.064 volt and the activity 10-fold in the ORR accelerated degradation test (ADT) in 5000 cycles. Besides, these NPs reduce noble metal loading by more than ~90%, as compared to that of commercial carbon supported Pt NPs. Such a design provides possible assessments for developing AFCs with high operating voltage and ultra-low noble metal loading. The atomic configurations in relation to ORR performances of NPs are introduced in the following sections.

Experimental

Synthesis of Pd, Ru–Pd, and Pt intercalated Ru_{core}–Pd_{shell} NPs

The Pd NPs (denoted as Pd) were synthesized using a polyol reduction method in the presence of 10 wt% polymer stabilizers (polyvinylpyrrolidone, PVP-40, MW ~ 42 000, 99%, Sigma-Aldrich) in ethylene glycol (EG, 99%, Acros) at 160 °C for 2 h. The Pd metal powder was dissolved in an aqueous solution of 1.0 M nitric acid, resulting in the Pd precursor. The Ru–Pd NPs (denoted as Ru–Pd) were synthesized by a dual-step polyol method. First, an hcp Ru core crystal (D_{avg} = 2.5 nm) was prepared by reducing 100 mM ruthenium chloride ($RuCl_3 \cdot 3H_2O$, 99.0%, Sigma Aldrich) in EG (denoted as PVP-Ru/EG). The Pd crystal was grown at the Ru core in the second polyol reduction in the PVP-Ru/EG solution (30 g) containing 10 mM of Ru. In this step, the Pd precursor (prepared by dissolving the Pd metal powder in EG in the presence of 1.0 M $HNO_{3(aq)}$) was dropped into the PVP-Ru/EG solution until the molecular ratio of Pd/Ru = 1.0. After stirring at 250 rpm for 3 min, the mixture was heated to 160 °C for 2 h to form Ru–Pd NPs. For preparing the Pt intercalated $Ru_C@Pd_S$ (denoted as $Pt/Ru_C@Pd_S$) NPs, an EG solution of 10 g PVP-blended Ru–Pd NPs (Pd = Ru = 10 mM) was mixed with an EG solution of a Pt salt ($H_2PtCl_6 \cdot 6H_2O$, 99%, Sigma-Aldrich) with the molecular ratios of Pt/Pd = 0.05 to 0.2. In this step, the surface defects of Ru–Pd are nucleation centres for catalysing the heterogeneous growth of Pt clusters and the restructuring of Ru–Pd into $Pt/Ru_C@Pd_S$. The pristine NPs were then dispersed into ethanol at a metal content of 1 mg (g^{-1}) as a slurry for the subsequent preparation of the electrode for the ORR activity test.

Preparation of the electrode for the ORR activity test

The slurry sample for the ORR experiment was made of 5.0 mg active carbon supported NCs which is a mixture of distilled water (14.0 mL), IPA (6.0 mL), and 5 wt% Nafion (0.1 mL). The mixture is stirred at 250 rpm for 30 min and then kept in an ultrasonication bath at 30 °C for 30 min. For preparing the working electrode in the ORR sweeping experiment, the slurry (20.0 μL) was dropped and dried on top of a rotation graphite electrode (diameter = 5.0 mm). The linear sweep voltammetry (LSV) data were collected using a potentiostat (CH Instruments Model 600B) equipped with a three-electrode electrochemical system. This system consists of a standard electrode of mercury oxide electrode (the voltage is calibrated by 0.098 volt in alignment to that of the RHE), a counter electrode of Pt metal wire, and a working electrode. The electrolyte is an aqueous solution of KOH (0.1 M). The voltage scan rate is 5 mV s^{-1} for LSV and 50 mV s^{-1} for the accelerated degradation test (ADT). In these electrochemical tests, the rotation speed of the electrode is 1600 rpm. For reducing the complexity of discussions, the structural characterizations are conducted only on the control sample and NCs with optimum electrochemical performances. The proposed structure to property correlations are clarified by comparing results of the electrochemical surface test before and after the ADT.

Catalyst characterization

The physical properties of experimental NPs were shown by microscopic (HRTEM) and spectroscopic (SAXS and UPS) characterizations at the electron microscopy center of National Sun Yat-Sen University and beamlines (BL-23A and BL-24A) at the National Synchrotron Radiation Research Center (NSRRC), Taiwan, respectively. The XRD patterns were collected at the beamline of BL-12B2 at Spring-8, Japan (data not shown). The XPS measurements were performed at the soft X-ray beamline (BL-24A1) of NSRRC. Different incident photon energies (PE) ranging from 440 to 1040 eV were implemented to probe the depth profiles of the composition of NPs (from 1.0 to 4.2 nm, which is calibrated by the kinetic energy of the photoelectrons from selected element orbitals). The probing depth was estimated by using the effective attenuation length (EAL) or inelastic mean free path (IMFP) methods.[17–20] We assessed

Published on 04 November 2016. Downloaded by Synchrotron Radiation Library on 11/09/2017 07:29:11.

empirical calibration constants of the atomic sensitivity factor (ASF), subshell ionization cross-section of the element, and the instrumental parameters of the analyser. The obtained results reveal that the emission peak areas are relatively proportional to the element concentration at the spectrum collected at select probing depths (PE). The use of the same photo-electron kinetic energy can yield sample depth information for all the elements. Those four excitation photon energies allowed us to have a similar photo-electron kinetic energy (350 eV, 550 eV, and 750 eV) for three elements. The details of the experimental parameters are given in the ESI.†

Density functional theory (DFT) simulations

Theoretical calculations were performed using the Vienna *ab initio* simulation package (VASP) based on DFT.[21–23] Projector augmented-wave (PAW) potentials were used to describe the core electrons. A generalized gradient approximation (GGA) in the form of Perdew–Wang 1991 formulation (PW91)[24–26] was adopted to describe the exchange–correlation function, which was developed by the surface system calculation. The properties of the Pd surface were simulated in the supercell of a 4×4 slab model with 5 atomic layers of the (111) facet. The Ru–Pd model was built on the supercell of the 4×4 slab of 3 atomic layers of Ru(001) facets capped by 2 atomic layers of Pd(111) facets following the symmetry of the Ru(001) substrate. For building the Pt/Ru_C@Pd_S model, the supercell of Ru_C@Pd_S was set as the sub-layer slab and 4 Pt atoms were substituting (subsurface, surface) Pt to (4,0), (3,1), (1,3) and (0,4) configurations, denoted as 40-Pt, 31-Pt, 13-Pt, and 04-Pt, respectively. The DFT results for the Pd, Pd/Ru(001), and Pd/Ru(001) with 4 Pt atom modification models are compared in Fig. 4 (electron distribution profiles) and ESI in Fig. S1† (density of states). The configuration of these models was determined by structural characterization of the experimental NPs. In this calculation, the vacuum region was set to 15 Å with minimized potential interference between the top and bottom surfaces of the periodic slab. Finally, the cut-off plane-wave expansion was taken to be 300 eV with the projector-augmented wave method (PAW)[27,28] and the Monkhorst–Pack mesh[29] of *k*-points for the irreducible Brillouin zone (IBZ) was chosen to be a 0.05×2 ($Å^{-1}$) interval in the reciprocal space. The structure was optimized until the energy and net force on every atom were smaller than 10^{-4} eV and 0.01 eV $Å^{-1}$, respectively.

Results and discussion

Nanostructure determination

The nanostructures of the Pt/Ru_C@Pd_S are determined through HRTEM, SAXS, and XPS depth profile analyses. The particle shape, surface configuration, and crystal structure of the NPs were elucidated using HRTEM. As shown in Fig. 1a, Pd is grown into a single crystallite with preferential orientation in the (111) facet ($d_{(111)_Pd} = 2.25$ Å) at the longitudinal axis (denoted by double yellow arrows). These NPs have a cylinder-like shape containing a high density of kinks and terrace defects in the surface region (denoted by green arrows). In Fig. 1b, Ru–Pd is grown in a polymorph of ellipsoid or cylindrical shape. The distinct truncations on the NPs (denoted by yellow arrows) confirm the preferential growth of the Pd crystal on top of the Ru core. A high roughness surface can be formed by growing Pd atoms at the Ru core surface *via* the heterogeneous nucleation-growth pathway in the presence of a strong lattice mismatch.[30] The inter-planar spacing is 2.08 Å, indicating the growth of the shell crystal with the Pd atoms in the hollow sites of Ru(001) facets (denoted by white triangles in Fig. S2†) at the longitudinal axis of NPs. This value is 7.5% smaller than that of Pd(111) facets ($d_{(111)} = 2.25$ Å) implying the formation of a metastable Pd shell crystal on the Ru core. In this case, two lattice planes of the shell Pd crystal ((111) and (110) facets) with a similar symmetry to that of Ru(001) and (200) facets are formed by different lattice strains. The preferential growth of the Pd crystal at the Ru core at different rates results in polymorphs of Ru–Pd. For Pt/Ru_C@Pd_S (Fig. 1c), the NPs are grown into multifaceted spherical crystallites with twin boundaries between Pd(111) facets in different directions (indicated by red arrows). In this case the lattice space at twin facets is 2.14 Å. This value is reduced by 4.5% compared to that of the Pd(111) facet, indicating the formation of a semi-coherent core–shell interface with strong compression strain in the Pd shell region. In addition, the Pt/Ru_C@Pd_S grows into spherical NPs (which is consistently proved by SAXS analysis later), indicating the restructuring of Pd atoms from the rocky face facet regions to the flat radial facets by intercalation of Pt clusters to the Ru_C@Pd_S.[31]

The nanostructure of experimental NPs is further confirmed using SAXS analysis. Fig. 2a compares the SAXS spectra [$I(q)$ *vs.* q] of the experimental NPs. In these spectra, the features in the q range <0.08 $Å^{-1}$ (region A) are derived from the inter-particle fractal dimension and the surface roughness of Pd. Given that the NPs were dispersed on carbon nanotubes prior to SAXS analysis, the effects of the fractal aggregate on the spectra can be ruled out. In this case, as consistently revealed by HRTEM (Fig. 1a) the largest slope (denoted by S) in the low q range illustrates the highest surface roughness of Pd among experimental NPs. The scattering oscillations in region B ($q > 0.08$ $Å^{-1}$) are interferences of the intra-particle structures (*i.e.* particle shape, average size, and configuration). As depicted, the indistinct scattering hump (0.15–0.35 $Å^{-1}$ as marked by the blue square in Fig. 2a inset) is due to the edge smearing effect of Pd and the polymorph of Ru–Pd (as probed by HRTEM images in Fig. 1) with a large polydispersity ($\rho = W/D_{all}$) of the particle size (Fig. 2b) on the SAXS feature. For Pt/Ru_C@Pd_S, a distinct scattering hump (denoted by arrow X) with considerable intensity (H) is found from 0.2 to 0.31 $Å^{-1}$ (denoted by W), resulting in the SAXS features of spherical NPs.

The structural parameters for experimental NPs are obtained by fitting their SAXS spectra in an adequate model (*i.e.*, poly-dispersed cylinder for Pd and poly-dispersed core–shell cylinder for Ru–Pd and Pt/Ru_C@Pd_S) and the obtained results are summarized in Table 1. Accordingly, Pd possesses an average diameter (D_{avg}) and length (L_{avg}) of 4.26 and 5.69 nm, respectively, with a ρ of 24.7%. The Ru–Pd is grown in cylinder-like-particles with a ρ of 23.5%. The core diameter (D_{avg}) and

 This journal is © The Royal Society of Chemistry 2016

Published on 04 November 2016. Downloaded by Synchrotron Radiation Library on 11/09/2017 07:29:11.

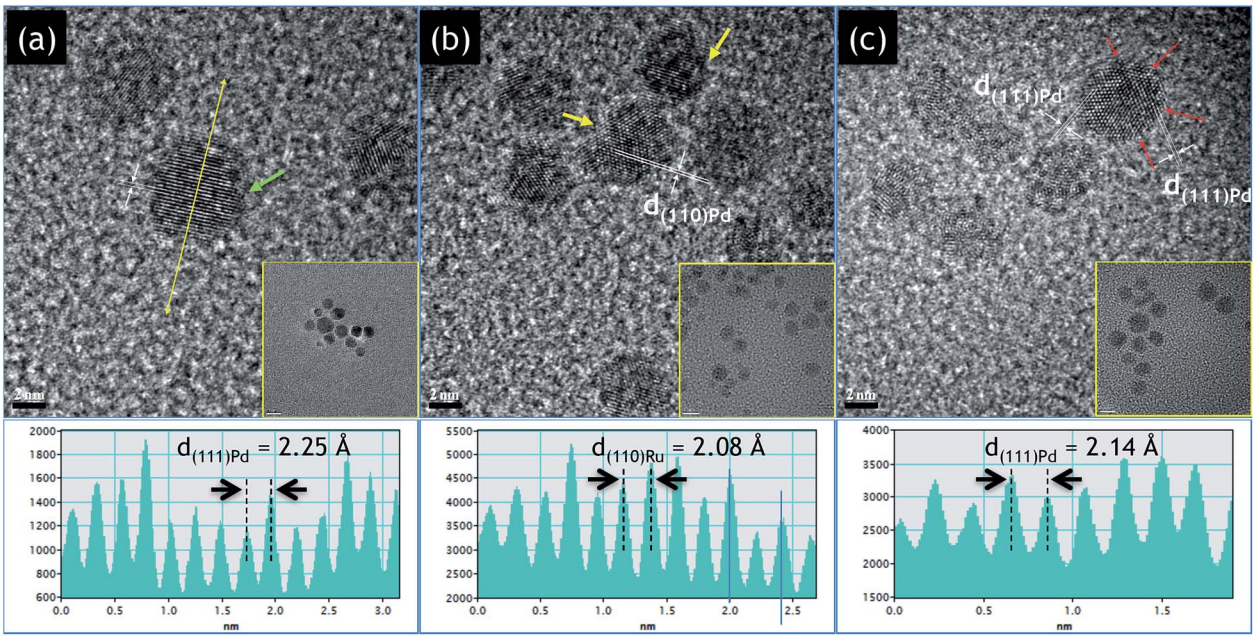

Fig. 1 HRTEM images of (a) Pd, (b) Ru–Pd, and (c) Pt/Ru_C@Pd_S NPs. Accordingly, Pd NPs grow into rod-like crystals with a high density of kinks and terrace defects in the surface. Ru–Pd grows into a polymorph of ellipsoid or cylinder shape with a cluster-at-cluster structure. Pt/Ru_C@Pd_S NPs tend to form spherical particles consisting of a Ru core and Pd shell due to the restructuring between Pt and Pd atoms in the particle surface.

length (L_C) are 2.70 and 2.04 nm, where the thicknesses of the radial shell (T_R) and face shell (T_F) are 0.2 and 5.28 nm, respectively. These parameters suggest the preferential growth of Pd at face facets of the core crystal. For determining the structural parameters of Pt/Ru_C@Pd_S, the Ru–Pd model is set as the core region (with a scattering length density of Pd and Ru in the molecular ratio of Pd/Ru = 1.0) and the Pt crystal is set as the shell region in the scattering model. In this case the D_{avg} and L_{avg} of Pt/Ru_C@Pd_S are 3.56 (with a D_C of 3.46 nm) and 3.65 nm. Meanwhile, the T_R and T_F are 0.26 and 0.1 nm, respectively. It is important to note that the Pt/Ru_C@Pd_S is grown into spherical NPs with an aspect ratio (D_{avg}/L_{avg}) of 0.97, suggesting the restructuring of Pd atoms to radial facets. Such a restructuring can be rationalized by the pathways of heterogeneous epitaxy growth in liquid states *via* the etch (transmetalation)–deposition cycle of relocation between Pd and Pt atoms in Scheme 2. In this process, the Pd restructuring involves four redox pathways, resulting in the Pt/Ru_C@Pd_S: (1) dissolution of Pd atoms at corners of face facets with transmetalation between Pd and $P{:}Pt^{4+}$ ($P{:}Pt^{4+} + 2Pd^C \rightarrow 2P{:}Pd^{2+} + Pt/Pd(111)^C$, where $P{:}Pt^{4+}$ and $P{:}Pd^{2+}$ denote the pyrrolidone ligand chelated Pt and Pd complexes); (2) halogen and protonation etching of corner/dangling Pd (Pd^C) atoms ($2Cl^- + Pd^C \rightarrow P{:}Pd^{2+}$ and $2H^+ + Pd^C \rightarrow P{:}Pd^{2+} + H_{2(g)}$); (3) thermal reduction of

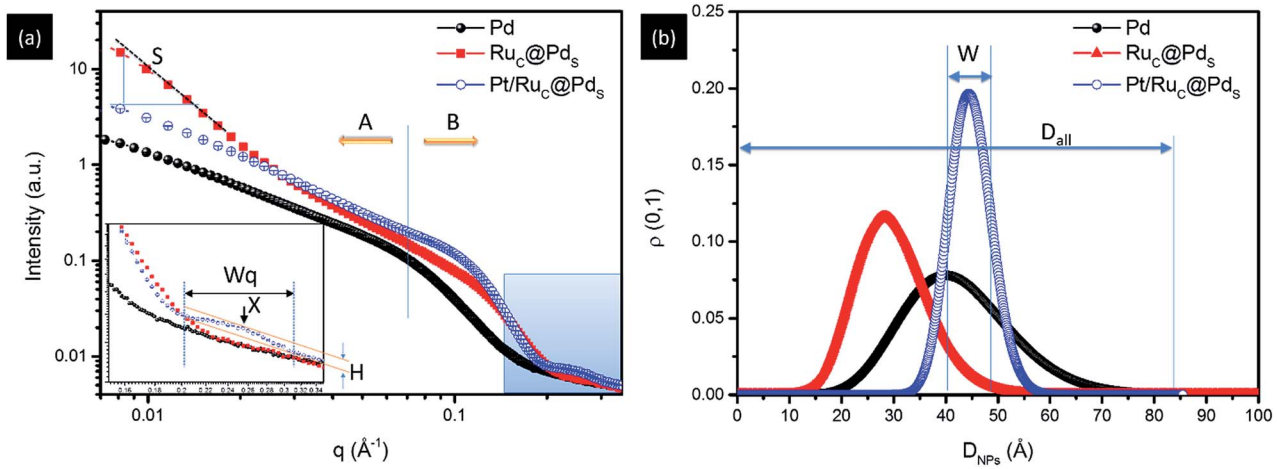

Fig. 2 (a) SAXS spectra of Pd, Ru–Pd, and Pt/Ru_C@Pd_S NPs and (b) the corresponding polydispersity of the particle size distribution. The scattering hump in the high q range supports the finding of HRTEM that most of the Pt/Ru_C@Pd_S NPs are grown in spherical core–shell NPs. The narrowed ρ is the direct indication of the high uniformity of Pt/Ru_C@Pd_S in the core–shell structure.

Published on 04 November 2016. Downloaded by Synchrotron Radiation Library on 11/09/2017 07:29:11.

Table 1 SAXS determined structural parameters of Pd, Ru–Pd and Pt/Ru_C@Pd_S NPs

NP	D_C[a] (nm)	D_{avg} (nm)	T_F (nm)	T_R (nm)	L_C (nm)	L_{avg} (nm)
Pd		4.25	NA	NA	NA	5.69
Ru–Pd_S	2.70	2.99	5.28	0.20	2.04	12.61
Pt/Ru_C@Pd_S	3.03	3.56	0.10	0.26	3.46	3.65

[a] D_C, D_{avg}, T_F, T_R, L_C, and L_{avg} denote the diameter of the core crystal, the diameter of nanoparticles, the thickness of the shell at face facets, the thickness of the shell at radius facets, the length of the core crystal, and length of nanoparticles in the longitudinal axis, respectively.

$P:Pd^{2+}$ at radial facets of the Ru core ($P:Pd^{2+}$ + CHO: + *Ru(200) → Ru(200)@Pd), where *Ru(200) and CHO: denote the activated Ru hollow sites at (200) facets for allocating Pd atoms and glycol radicals, respectively; (4) simultaneous thermal reduction of $P:Pd^{2+}$ and $P:Pt^{4+}$ into $Pt^{cluster}$ at the Pd shell by CHO: ($P:Pt^{4+}$ + CHO: + *Ru(200) → $Pt_X^{cluster}$/Ru(200)@Pd, $X \ll 1$). In these steps, the Pd shell is formed prior to the Pt clusters due to their substantial lower surface energy in comparison with Pt metal. In addition to the Pd restructuring, ρ is 9.1% denoting the growth of Pt/Ru_C@Pd_S in the core–shell structure with high uniformity.[32]

According to HRTEM and SXAS analysis, modification of atomic Pt clusters transforms the cluster-in-cluster structured Ru–Pd into Pt decorated Ru_C@Pd_S NPs. In determining the chemical distribution of experimental NPs, the depth profile of X-ray photoemission spectroscopy is employed. The representative XPS spectra with fitting curves at Pt 4f, Pd 3d, and Ru 3d orbitals were collected at different excitation energies of incident photons, which are given in Fig. S3.† This technique determines the chemical distributions of NPs at different probing depths. In Fig. S3a,† the two emission lines at 71.1 and 74.5 eV originate respectively from Pt $4f_{7/2}$ and $4f_{5/2}$, where the inelastic stepped background was fitted by a pseudo-Voigt equation and the area ratio of Pt $4f_{5/2}/4f_{7/2}$ peaks was set to be 0.75.[33] By increasing the PE from 440 to 1040 eV (probe depth) the area of the two emission peaks decreased by 67%, indicating a reduction of Pt content with increasing depth. On the other hand, the areas of Ru and Pd 3d emission peaks progressively increased in this PE region. The photoemission quantitation analysis (Fig. S3†) reveals that the relative composition of Pt was determined from 2.2 to 3.4 at% upon increasing the kinetic energy of emission photoelectron "KE" from 350 to 750 eV. Given that the emission line intensity of high KE photoelectrons is convolution of the signal from the bulk and surface of NPs, the composition of the core crystal is a difference of the NP surface and the sum. These results suggest the composition profile of Pt at 2.2, 0.6, and 0.6 at% relative to the probing depth of ~2.4, ~3.6, and ~4.2 nm, respectively. These features elucidate the growth of Pt clusters in the surface region of Ru_C@Pd_S.

Effects of atomic cluster modification on valence band structures of experimental NPs

The intercalation of atomic clusters adds a localized heterojunction to Ru–Pd. These Pt clusters induce a strong electron injection and thus boost the oxygen reduction activity of NPs.

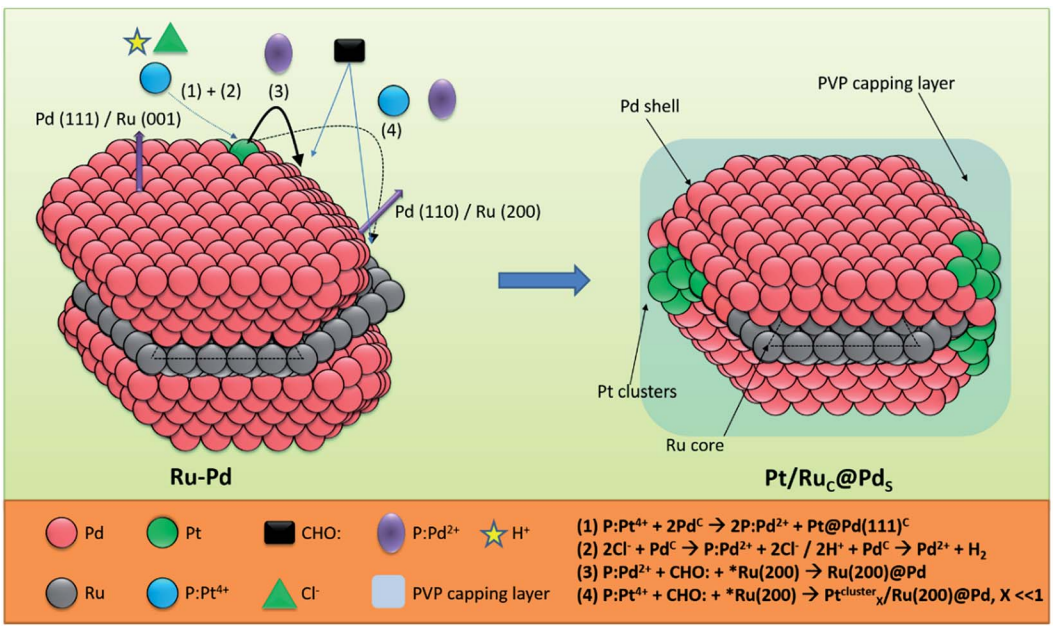

Scheme 2 The schematic representation of etch–deposition based liquid state epitaxy growth for the Pd relocation by interaction with Pt^{4+}, H^+, and Cl^- in the polyol reaction.

 This journal is © The Royal Society of Chemistry 2016

Published on 04 November 2016. Downloaded by Synchrotron Radiation Library on 11/09/2017 07:29:11.

The electron injection effects are consistently demonstrated by VB analysis and DFT calculations. Fig. 3 compares the VB spectra of active carbon supported Pd, Ru–Pd, and Pt/Ru_C@Pd_S NPs (coating on FTO), where the intensity of the VB below the Fermi level (E_F) is normalized to the same value. Fig. S4a† shows the VB spectra of Ru and Pt NPs as a reference. As indicated in these figures, there is a substantial modification between reference and experimental NPs. These changes resemble the coupling effects of the sub-layer crystal (the Ru core in this study) with the VB structures of the Pd shell crystal and the Pt clusters in the outmost layer. In Fig. 3, the VB of NPs comprises several regions: (A) a descent from 0.00 to 0.51 eV, an inflection point at 1.00 eV (*i.e.*, the surface binding energy, E_b), and a second rise with a steep slope to 3.05 eV; (B) a broad band from 3.05 to 11.3 eV with three peaks at 4.29, 8.95 and 10.80 eV; and (C) a valley centred at 12.13 eV. The electrons below the E_F (in region A) refer to the relative amount of density of states (DOS) on the experimental substrate (NPs). For Pd, a slide from 3.05 to 1.0 eV with a significant intensity drop indicates prevalent empty states in the outermost band. This open valence state is caused by the chemisorption of oxygen on the metal surface. In region B, a steep slope from 3.05 to 4.29 eV (peak B1) typifies the presence of a potential gap which localizes the electrons in the interface between the distorted metal and metal oxide near the NP surface. In the high energy region, the bandwidth is expanded to 11.3 eV and split into B2, and B3 at 8.95 and 10.80 eV, respectively. These distinct features are similar to those of metallic Pd at various facets with different extents of oxidation.[34,35] The features in region C (where intensity is progressively increased at BE above 11.9 eV) are photoemission signals from near-core-levels (Fig. S4a†).

There is a slight increase of intensity in region A with identical VB features in high energy regions (regions B and C) in the VB spectrum, as compared to that of Pd. These characteristics indicate the preservation of valence electrons at the PdO/Pd shell with electron donation from the Ru crystal. Compared to that of Ru–Pd, a quantum leap of intensity is found in region A of Pt/Ru_C@Pd_S. These novel characteristics resemble a significant valence charge injection to the heterojunction of Pt clusters in the Pd-shell. This hypothesis is further confirmed by the VB features in the high binding energy region (region B). As clearly indicated, the intensity of the VB peak is substantially reduced by 20% with the position downshifted by 0.2 eV (from 4.4 to 4.2 eV). The energy downshift and the shape modification of these split bands again prove the occurrence of anti-oxidation shielding and the electron relocation by Pt clusters in the Pd shell. As verified by our DFT calculations (Fig. S1†), the atomic Pt clusters extract the valence electrons from the sub-layer crystallite underneath to near the E_F level (region A) to form a negative potential field at the NPs. This VB restructuring is caused by (i) the electronegative difference between the Pt cluster and neighbouring crystal and (ii) the coupling effects between the two. The VB features of Pt/Ru_C@Pd_S demonstrate some advantages of the surface reduction reaction of NPs. In region A, the prevailing DOS indicates a sufficient amount of electrons, which interact with molecules chemisorbed on the NP surface. These characteristics indicate a considerable amount of valence charge injection from Ru–Pd to Pt and the localization of these electrons in the sub-core level region due to the strain inducing interfacial Pt–Pd coupling. The flattened region B indicates the reduced energy barrier for relocating the VB electrons to the outmost states. These two features refer to the presence of negative potential fields that substantially enhance the electron–hole recombination rate for oxygen reduction at NPs.

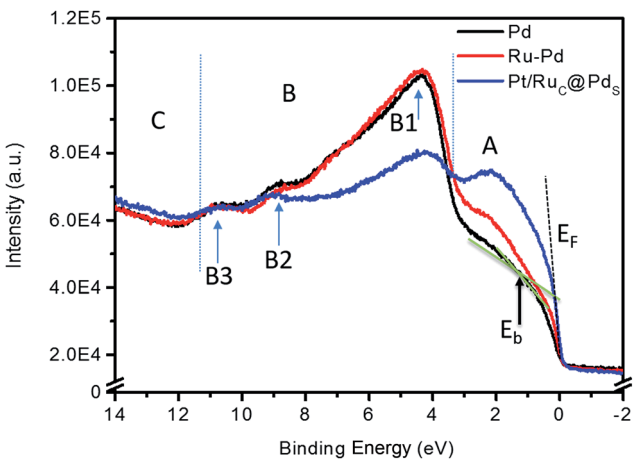

Fig. 3 Valence band spectra of active carbon supported Pd, Ru–Pd, and Pt–Ru_C@Pd_S NPs at FTO.

Cluster induced charge relocation on experimental NPs

The effects of local strain and heterojunction coupling on the VB electron relocations are confirmed by DFT calculation of the models of 40-Pt, 31-Pt, 13-Pt, and 04-Pt (Fig. 4). Note also that the stack configuration of the Pt clusters dominates the DOS features of these models.

Shown in Fig. 4 is the DFT calculated induced charge density distribution profiles of assigned models according to structural characterization. These models illustrate the electron relocation patterns that are triggered by the Pt clusters in different configurations in the Pd shell of Ru_C@Pd_S models consisting of Ru (001) facet slab capping with two atomic layers of Pd atoms. The pink and green spheres represent the Pd and Pt atoms, respectively, in the shell region. Note that Ru atoms in the sublayer "core" region are not shown in this figure. The red and blue isosurfaces indicate depletion (−) and addition (+) regions, respectively, of the induced charge 0.02 $|e|/Å^{-3}$ by Pt clusters. The induced charge density is determined by subtracting the charge density of the isolated Pt cluster and Ru(001)@Pd from that of optimized Pt cluster-intercalated Ru(001)@Pd. Accordingly, a substantial charge separation is found on Pd atoms around the Pt cluster, which is denoted by the direction of yellow arrows. The electron rich area (blue isosurfaces) is remarkable, suggesting the significant charge localization in the interface between the Pd shell and Pt cluster. This phenomenon is further confirmed by the depletion and rich areas of electrons in the centre and edge of the Pt cluster. By restructuring the Pt atoms onto the Pd outmost layer, the blue sphere in the interface (blue arrows) and green isosurfaces at

Published on 04 November 2016. Downloaded by Synchrotron Radiation Library on 11/09/2017 07:29:11.

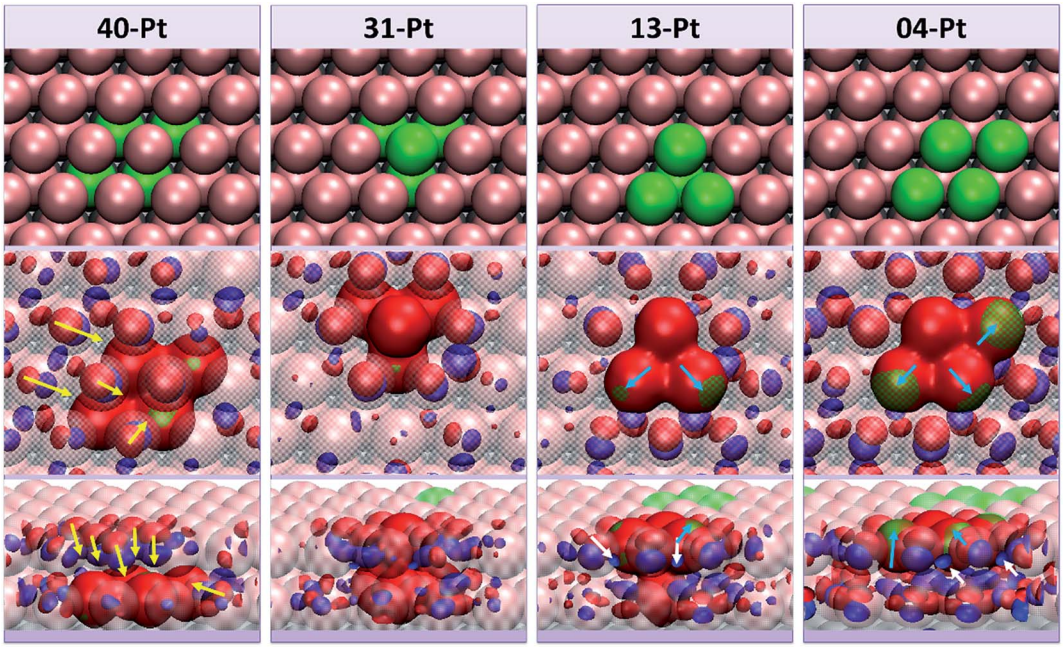

Fig. 4 The DFT calculated charge density distributions of the Ru(001)@Pd model with 4-atom Pt clusters in different configurations, the models of 40-Pt, 31-Pt, 13-Pt, and 04-Pt (scheme for the heterojunction induced electron relocation in 40-Pt (c1), 31-Pt (c2), 13-Pt (c3), 04-Pt (c4), and $Pt^{cluster}$–Ru(001)@Pt (c5) and the corresponding density of states are shown in Fig. S4†).

the edge of Pt atoms (white arrows) illustrate the substantially enhanced charge relocation in 31-Pt, 13-Pt and 04-Pt as compared to that of 40-Pt. For the case of 04-Pt, the charge density around the Pt cluster is boosted to the largest extent among the existing models. This provides concrete evidence for the charge injection by the coupling effects in the interfaces between Pt–Pd–Ru heterojunctions. The results of the charge distribution and DOS (Fig. S1†) rationalize that the electron relocation is induced by a local compression strain (δ), electronegativity difference, and heterojunction coupling in the Ru–Pd interface. Also, the results indicate that the induced charge upon Pt intercalation is located near the Fermi level (DOS). The corresponding charge relocation pathways are given in the ESI.†

Effects of cluster induced charge relocation on the oxygen reduction activity of experimental NPs

Fig. 5a demonstrates the linear sweep voltammetry (LSV) spectra of Ru–Pd compared with $Pt/Ru_C@Pd_S$ with different Pt/Pd ratios (namely Pt-5, Pt-10, and Pt-20 with respect to NCs containing Pd/Ru = 1 and Pt/Rd = 5, 10, and 20 at%) and commercial carbon supported Pt (JM Pt/C). In this analysis system, the electrolyte is an O_2-saturated KOH solution (0.1 M) and the rotation speed of the working electrode is 1600 rpm. As illustrated, the onset potential (V_{OC}) of NPs under investigation follows the trend: Pt-20 (a at 0.954 volt) > Pt-10 (a at 0.950 volt) > Pt-5 (b at 0.935 volt) > Ru–Pd (c at 0.903 volt). Their mass activities (MA, current densities *vs.* Pt metal loading) also have the same sequence at 0.85 volt (Table 2). In addition, compared to that of Ru–Pd, current density at 0.85 volt is increased by ~122% (from 0.35 to 0.78 mA cm^{-2}) by adding 5 at% of Pt (*vs.* Pd). By increasing Pt to 10 and 20 at% (*vs.* Pd), the current density of NCs is further increased by ~274% (0.35 to 1.31 mA cm^{-2}) and ~282% (0.35 to 1.34 mA cm^{-2}). For clarifying the location of Pt in NCs, the chemical selective electrochemical analysis by carbon monoxide stripping is conducted (Fig. S5a†). Accordingly, compared to Pt/C (commercially available carbon supported Pt catalyst), the position of the CO oxidation peak of Pt-5 is shifted by a maximum extent of 0.11 volt (0.78 to 0.67 volt) accompanied by the largest current drop of ~28% (6.5 to 4.7 mA cm^{-2}) and the lowest onset potential (568 mV) showing its highest CO oxidation activity among the current NCs. These characteristics indicate the promotion of ORR activity on $Pt/Ru_C@Pd_S$ by Ru to Pt coupling induced charge localization around Pt clusters instead of the increasing intrinsic ORR activity of Pt with the metal loading (also proved by the ORR activity of Pt doped Pd core NPs in Fig. S6 and Table S3†). The enhanced ORR activity upon Pt addition can be understood from the DOS analysis in the DFT calculation. The Pt addition moves the d band to lower energies (Fig. S1†) that can lower the oxophilicity (adsorption energy of oxygen-containing adspecies) and improve ORR activity. Also, the induced charge analysis in the DFT calculation (Fig. 4) indicates that the Pt induced negative charge on the surface will weaken the adsorption energy of oxygen-containing species, the key intermediate in the ORR, and improve the ORR activity. Fig. 5b shows the accelerated degradation test results of experimental NCs. As indicated, the current density of Ru–Pd is progressively decreased by ~47% (from 0.38 to 0.205 mA cm^{-2}) with increasing ADT until 5000 cycles. For investigating the effects of Pt loading, MA is normalized by this factor (denoted as $MA_{0.85(Pt)}$) and the results are summarized in Table 2. As

 This journal is © The Royal Society of Chemistry 2016

Published on 04 November 2016. Downloaded by Synchrotron Radiation Library on 11/09/2017 07:29:11.

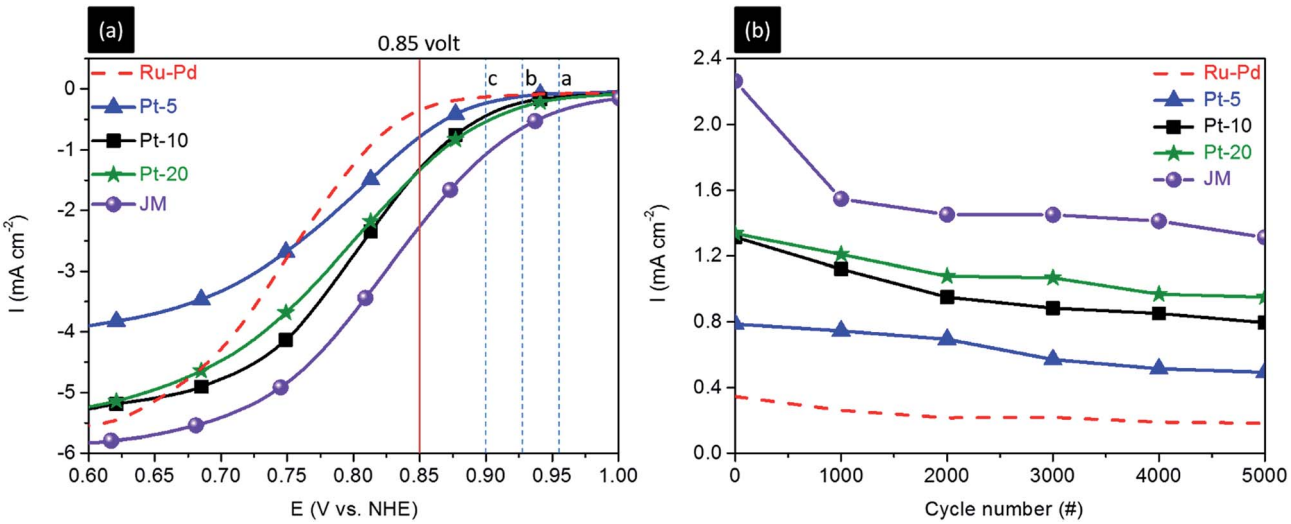

Fig. 5 (a) Linear sweep voltammetry (LSV) spectra of Ru–Pd compared with $Pt/Ru_C@Pd_S$ with different Pt/Pd ratios (namely Pt-5, Pt-10, and Pt-20 with respect to NCs containing Pd/Ru = 1 and Pt/Rd = 5, 10, and 20 at%) for oxygen reduction and (b) the corresponding accelerated degradation test.

depicted, the $MA_{0.85(Pt)}$ of Pt-5 is 1643 (mA mg_{Pt}^{-1}). This value is the highest one among NCs under investigation and is degraded by 37.3% (to 1030 (mA mg_{Pt}^{-1})) in the ADT. The corresponding CO stripping analysis (Fig. S5b–d†) proves that this phenomenon is accounted for by the restructuring of Pt into the NP core region (revealed by restructuring on CO stripping curves of Pt-5, -10, -20 after the ADT) or possibly dissolution of Pt/Pd atoms in the electrolyte. Such a hypothesis can be rationalized by the unstable structure of Pt atoms at the terrace site.

By increasing Pt/Pd to 20 at% (Pt-20), the initial $MA_{0.85(Pt)}$ is decreased to 698 (mA mg_{Pt}^{-1}) due to the decrement of highly reactive defect sites by capping with Pt atoms in the NP surface. After the ADT, it shows the lowest $MA_{0.85(Pt)}$ degradation of 28.9% (from 698 to 496 (mA mg_{Pt}^{-1})) among the NPs under investigation. The suppressed degradation can be attributed to a considerable extent of surface coverage at surface defects by strong atomic bonds of Pt cluster intercalation. These Pt clusters increase the heteroatomic alloying and thus reduce the dissolution followed by relocation of atoms in the NP surface in the ADT. In this event, the inter-particle agglomeration is substantially suppressed in Pt-20 (Fig. S7†). In this case, reduction of Pt coverage suppresses surface dissolution of NPs in the ORR. This phenomenon facilitates the inter-particle agglomeration, and therefore, increases the MA degradation of Pt-10 and Pt-5. In addition, the charge transfer number is 3.8 (Table S3†) indicating that the passivation effects of by-products make certain contributions to the MA decay of Pt-20 in the ADT. Such a phenomenon rationalizes the considerable MA degradation (28.9%) without substantial inter-particle agglomeration of Pt-20 (Fig. S7†). For NPs containing Pt less than 2 at% (*i.e.*, Pt-10 and Pt-5) and commercial standard JM Pt/C, the MA degradation is mainly accounted for by the inter-particle agglomeration in the ADT. The same trend is found for the MA of the total metal for all NPs (denoted as $MA_{0.85_total}$ in Table 2); where the initial $MA_{0.85_total}$ of Ru–Pd NPs is improved by 345% (from 180 to 801 (mA mg^{-1})) when intercalating Pt atoms in a ratio of Pt/Pd = 5 at% (*i.e.* a total of ~2 at% in NPs) in $Pt/Ru_C@Pd_S$ NPs. After the ADT for 5000 cycles, the difference of $MA_{0.85_total}$ between Pt-5 and Ru–Pd is further increased to 390% (from 85 to 502 (mA mg^{-1})) again proving the reinforcement of the NP structure by surface Pt clusters.

Table 2 Electrochemical parameters of $Pt/Ru_C@Pd_S$ NPs compared with Ru–Pd NPs and standard carbon supported Pt (JM Pt/C) in the accelerated degradation test in the oxygen reduction reaction

			$MA_{0.85(Pt)}$ (mA mg^{-1} Pt)		$MA_{0.85_total}$ (mA mg^{-1})		
Sample	E_{onset} (volt *vs.* RHE)	$I_{0.85}$ (mA cm^{-2})	1st	5000th	1st	5000th	MA decay (%)
Pt-5	0.935	0.78	1643	1030	801	502	37.3
Pt-10	0.950	1.31	1374	838	654	399	39.0
Pt-20	0.954	1.34	698	496	317	225	28.9
Ru–Pd	0.903	0.35	NA[a]		180	85	47.2
JM Pt/C	0.913	2.45	67				34.8

[a] No Pt content in the catalyst, $I_{0.85}$ is determined at a rotation speed of 1600 rpm.

Published on 04 November 2016. Downloaded by Synchrotron Radiation Library on 11/09/2017 07:29:11.

Conclusions

In this work, the intercalation of atomic scale Pt clusters is employed for synthesizing Pt cluster modified $Ru_C@Pd_S$ NPs as electrode catalysts in oxygen reduction application. We demonstrate that the Ru–Pd NPs will be restructured into $Ru_C@Pd_S$ NPs with modified Pt atomic clusters when they interact with Pt ions. These Pt clusters induce electron injection from the core–shell heterojunction. With physical structure inspections and theoretical DFT calculations, we found that electrons are injected to these Pt clusters and are localized at the near-Fermi level of the NPs. In addition to the electron redistribution in VB states, the local strain lowers the energy barrier for extracting electrons from the near-core level to the near Fermi regions. By formation of surface negative charge localization, the MA of O_2 reduction of the NPs is facilitated. For the optimum cases, MA and ADT degradation for the total metal of $Pt/Ru_C@Pd_S$ is improved by ~345% (Pt-5) and 17.3% (Pt-20) as compared to that of Ru–Pd NPs. Furthermore, the catalytic activity of the NPs being investigated is tuneable by changing the Pt cluster size and the core configurations. Most importantly, this work provides systematic structural characterizations, theoretical calculations and electrochemical analysis, for optimizing the utilization of noble metals in NPs and the performance of future alkaline fuel cell devices.

Acknowledgements

The authors thank the staff of National Synchrotron Radiation Research Center (NSRRC), Hsinchu, Taiwan for helping in various synchrotron-based measurements. The VASP based DFT calculations were performed and the results were obtained by using the clusters at the National Center for High-Performance Computing, Taiwan. The EDX map and HAADF images were observed by using a TEM-FEI Osiris platform with a four detector EDS system (Oxford) at MSSCORP CO., LTD. T.-Y. Chen acknowledges the funding support from the National Tsing Hua University, Taiwan (N103K30211 and 103N1200K3) and the Ministry of Science and Technology, Taiwan (MOST 103-2112-M-007-022-MY3 and MOST 105-3113-E-006-019-CC2).

Notes and references

1 M. Gratzel, *Nature*, 2001, **414**, 338–344.
2 C. Yasuo, I. Ashraful, W. Yuki, K. Ryoichi, K. Naoki and H. Liyuan, *Jpn. J. Appl. Phys.*, 2006, **45**, L638.
3 S. Ito, S. M. Zakeeruddin, R. Humphry-Baker, P. Liska, R. Charvet, P. Comte, M. K. Nazeeruddin, P. Péchy, M. Takata, H. Miura, S. Uchida and M. Grätzel, *Adv. Mater.*, 2006, **18**, 1202–1205.
4 E. Ghadiri, N. Taghavinia, S. M. Zakeeruddin, M. Grätzel and J.-E. Moser, *Nano Lett.*, 2010, **10**, 1632–1638.
5 M. Law, L. E. Greene, J. C. Johnson, R. Saykally and P. Yang, *Nat. Mater.*, 2005, **4**, 455–459.
6 M. A. Kostowskyj, R. J. Gilliam, D. Kirk and S. J. Thorpe, *Int. J. Hydrogen Energy*, 2008, **33**, 5773–5778.
7 C. Luo, H. Xie, Q. Wang, G. Luo and C. Liu, *J. Nanomater.*, 2015, **2015**, 560392.
8 C.-C. Hu and K.-Y. Liu, *Electrochim. Acta*, 1999, **44**, 2727–2738.
9 C.-C. Hu and K.-Y. Liu, *Electrochim. Acta*, 2000, **45**, 3063–3068.
10 G. T. Burstein, C. J. Barnett, A. R. Kucernak and F. R. Williams, *Catalyst Today*, 1997, **38**, 425–437.
11 M. Watanabe and S. Motoo, *J. Electroanal. Chem.*, 1975, **60**, 275–283.
12 M. Watanabe, M. Uchida and S. Motoo, *J. Electroanal. Chem.*, 1987, **229**, 395–406.
13 R. R. Adzic, J. Zhang, K. Sasaki, M. B. Vukmirovic, M. Shao, J. X. Wang, A. U. Nilekar, M. Mavrikakis, J. A. Valerio and F. Uribe, *Top. Catal.*, 2007, **46**, 249–262.
14 T. Y. Chen, T. L. Lin, T. J. M. Luo, Y. Choi and J. F. Lee, *ChemPhysChem*, 2010, **11**, 2383–2392.
15 T. Y. Chen, H. D. Li, G. W. Lee, P. C. Huang, P. W. Yang, Y. T. Liu, Y. F. Liao, H.-T. Jeng, D. S. Lin and T. L. Lin, *Phys. Chem. Chem. Phys.*, 2015, **17**, 15131–15139.
16 T. Y. Chen, Y. T. Liu, H. M. Nguyen, L. J. Fan, C. Y. Wu, T. J. Mark Luo, C. H. Lee, Y. W. Yang, T. C. Wen and T. L. Lin, *J. Mater. Chem. A*, 2013, **1**, 5660–5669.
17 C.-J. Powell and A. Jablonski, *NIST electron effective attenuation-length database Version 1.2*, Gaithersburg, 2001.
18 M. P. Seah and W. A. Dench, *Surf. Interface Anal.*, 1979, **1**, 2–11.
19 N. J. Divins, I. Angurell, C. Escudero, V. Pérez-Dieste and J. Llorca, *Science*, 2014, **346**, 620–623.
20 S. Ghosal, J. C. Hemminger, H. Bluhm, B. S. Mun, E. L. D. Hebenstreit, G. Ketteler, D. F. Ogletree, F. G. Requejo and M. Salmeron, *Science*, 2005, **307**, 563–566.
21 G. Kresse and J. Hafner, *Phys. Rev. B: Condens. Matter Mater. Phys.*, 1993, **47**, 558.
22 G. Kresse and J. Furthmüller, *Phys. Rev. B: Condens. Matter Mater. Phys.*, 1996, **54**, 11169.
23 G. Kresse and J. Hafner, *Phys. Rev. B: Condens. Matter Mater. Phys.*, 1994, **49**, 14251.
24 J. P. Perdew and K. Burke, *Phys. Rev. Lett.*, 1996, **77**, 3865.
25 J. P. Perdew, J. A. Chevary, S. H. Vosko, K. A. Jackson, M. R. Pederson, D. J. Singh and C. Fiolhais, *Phys. Rev. B: Condens. Matter Mater. Phys.*, 1992, **46**, 6671.
26 J. P. Perdew and Y. Wang, *Phys. Rev. B: Condens. Matter Mater. Phys.*, 1992, **45**, 13244.
27 P. E. Blöchl, *Phys. Rev. B: Condens. Matter Mater. Phys.*, 1994, **50**, 17953.
28 G. Kresse and D. Joubert, *Phys. Rev. B: Condens. Matter Mater. Phys.*, 1999, **59**, 1758.
29 H. J. Monkhorst and J. D. Pack, *Phys. Rev. B: Condens. Matter Mater. Phys.*, 1976, **13**, 5188.
30 M. Zinke-Allmang, L. C. Feldman and M. H. Grabow, *Surf. Sci. Rep.*, 1992, **16**, 377–463.
31 T. Bligaard and J. K. Nørskov, *Electrochim. Acta*, 2007, **52**, 5512–5516.
32 T.-Y. Chen, T.-L. Lin, T.-J. M. Luo, Y. Chio and J.-F. Lee, *ChemPhysChem*, 2010, **11**, 2383–2392.
33 M. Schmid, H.-P. Steinrück and J. M. Gottfried, *Surf. Interface Anal.*, 2014, **46**, 505–511.
34 P. Oelhafen, in *Rapidly Quenched Metals 6*, ed. R. Cochrane, Elsevier Sequoia, Netherland, 1988, p. 240.
35 T. Hofmann, in *Chemistry*, University of Nevada, Las Vegas, 2009, p. 124.

 This journal is © The Royal Society of Chemistry 2016